Parametric imaging of myocardial blood flow, innervation and metabolism using PET/CT

Harms, H.J.

2014

document version
Publisher's PDF, also known as Version of record

3

Automatic generation of absolute myocardial blood flow images using $[^{15}O]H_2O$ and a clinical PET-CT scanner

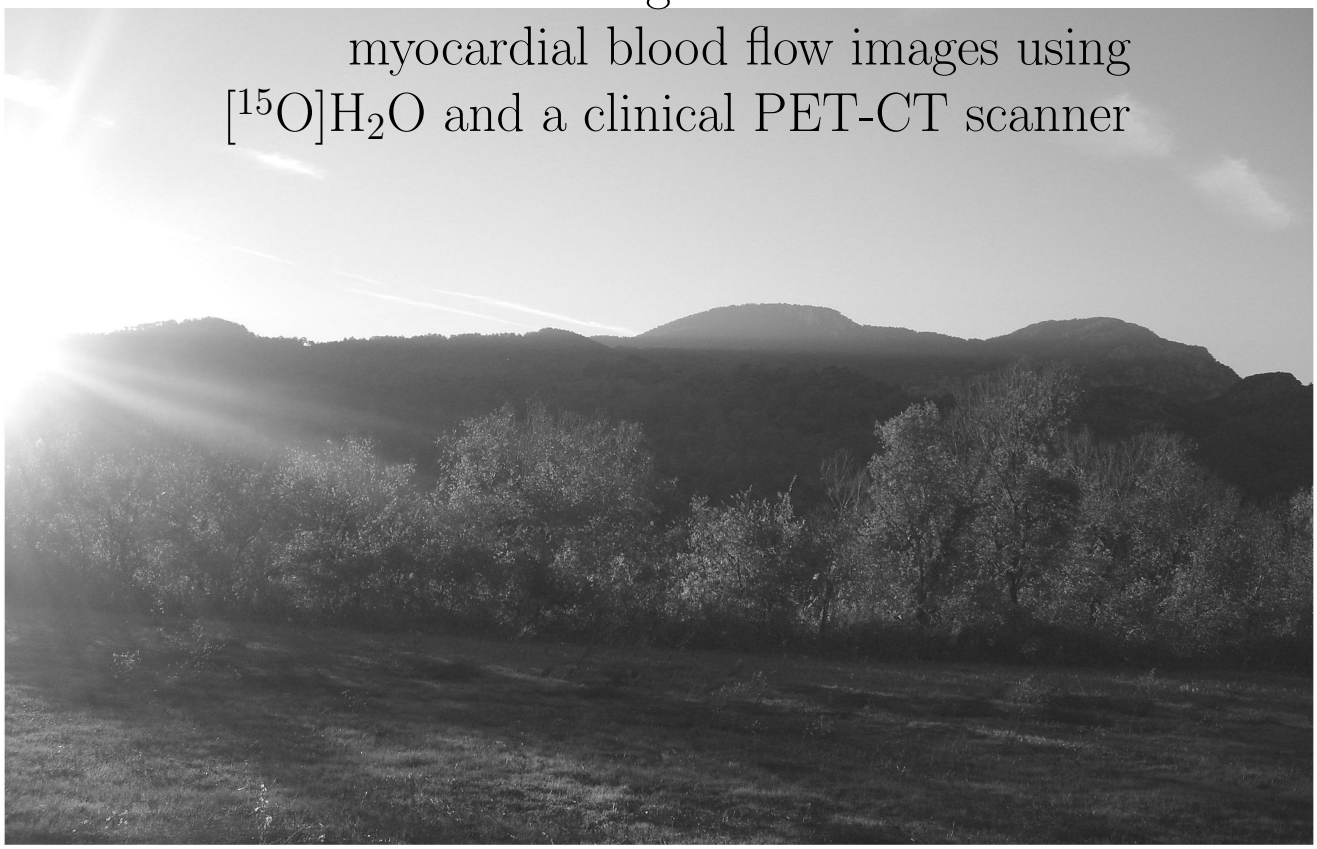

Hendrik J. Harms, Paul Knaapen, Stefan de Haan, Rick Halbmeijer, Adriaan A. Lammertsma and Mark Lubberink

This research was originally published in European Journal of Nuclear Medicine and Molecular Imaging. *Hendrik J. Harms, Paul Knaapen, Stefan de Haan, Rick Halbmeijer, Adriaan A. Lammertsma and Mark Lubberink. Automatic generation of absolute myocardial blood flow images using $[^{15}O]H_2O$ and a clinical PET-CT scanner. EJNMMI. 2011;38:930-939.*

Abstract

Parametric imaging of absolute myocardial blood flow (MBF) using $[^{15}O]H_2O$ enables determination of MBF with high spatial resolution. The aim of this study was to develop a method for generating reproducible, high quality and quantitative parametric MBF images with minimal user intervention.

Methods: 19 patients referred for evaluation of MBF underwent rest and adenosine stress $[^{15}O]H_2O$ PET scans. Ascending aorta and right ventricular (RV) cavity volumes of interest (VOIs) were used as input functions. A basis function (BFM) implementation of the single tissue model with an additional correction for RV spill-over was used to generate parametric images. Average segmental MBF derived from parametric images was compared with MBF obtained using nonlinear least-squares regression (NLR) of VOI data. Four segmentation algorithms were evaluated for automatic extraction of input functions. Segmental MBF obtained using these input functions was compared with MBF obtained using manually defined input functions.

Results: Average parametric MBF was highly correlated with NLR derived MBF ($r^2 = 0.964$, ICC = 0.984). For each segmentation algorithm there was at least one implementation that yielded high agreement (ICC > 0.9) with manually obtained input functions although MBF calculated using each algorithm was at least 10% higher. Cluster analysis with 6 clusters yielded the highest agreement (ICC = 0.977), together with good segmentation reproducibility (CoV of MBF $< 5\%$).

Conclusion: Parametric MBF images of diagnostic quality can be generated automatically using cluster analysis and a BFM implementation of the single tissue model additional RV spill-over correction.

3.1 Introduction

Dynamic positron emission tomography (PET) can be used to measure regional myocardial blood flow (MBF) non-invasively using for example $[^{13}N]NH_3$, ^{82}Rb or $[^{15}O]H_2O$ (9, 10, 15). The introduction of hybrid PET-CT scanners enables accurate diagnosis of coronary artery disease (CAD) by combining PET perfusion studies with CT coronary angiography (CTCA) (7, 21, 74, 149). Given the short half-life of ^{15}O and ^{8}Rb (122 s and 76 s, respectively), repeat scans are feasible within a single scanning session, enabling stress-rest-CTCA protocols with a total duration of less than 30 min. In contrast to ^{82}Rb and $[^{13}N]NH_3$, $[^{15}O]H_2O$ is freely diffusible and metabolically inert. Consequently, $[^{15}O]H_2O$ is an ideal tracer for quantifying MBF, as changes in myocardial tracer activity are solely dependent on MBF and are not affected by variations in extraction fraction and/or metabolic interactions (74). Kinetics of $[^{15}O]H_2O$ can best be described using a single tissue compartment model with parameters for MBF and, to correct for partial volume and spill-over effects, perfusable tissue fraction (PTF) (11, 12), and left (LV) and right (RV) ventricular blood volume fractions (107). Using least squares fitting techniques on segmental $[^{15}O]H_2O$ data, it has been shown that resulting MBF values correlated well with MBF based on microspheres using both 2D (11, 13) and 3D (72) PET data.

In order to solve the single tissue compartment model, time activity curves (TACs) of arterial blood and RV, $C_A(t)$ and $C_{RV}(t)$, respectively, have to be determined. It has been shown (13, 72, 107, 117) that $C_A(t)$ can be obtained accurately from the dynamic data itself, eliminating the need for on-line blood sampling. This can be achieved by drawing volumes of interest (VOIs) in ascending aorta (AA), left ventricle or left atrium, and RV in a blood pool image obtained using $[^{15}O]CO$ and transferring these VOIs to the dynamic $[^{15}O]H_2O$ data (117). Although the LV is often used to define the arterial input function for $[^{15}O]H_2O$, previous studies have shown that the AA is preferable for $[^{18}F]FDG$ (150). In addition, perfusion values based on an AA IDIF were shown to correlate well with those based on on-line arterial sampling (134). Performing an additional $[^{15}O]CO$ scan, however, is cumbersome and drawing VOIs is user dependent and time consuming. In addition, there is a chance of misalignment between blood pool and water scans due to patient movement. VOIs can also be drawn on the $[^{15}O]H_2O$ data themselves using a frame during the first pass of the bolus, where the blood pool is best visible. Although this eliminates errors due to patient movement between scans, it remains user dependent and time consuming. Therefore, automatic methods for extracting $C_A(t)$ and $C_{RV}(t)$ directly from a dynamic scan are preferred.

Factor analysis (119, 120) has been used to extract blood and tissue TACs from dynamic PET images. Factor analysis separates a small number of underlying and unobservable factors that define the dynamic data. Its use in combination with dynamic $[^{15}O]H_2O$ scans of the heart has been shown (125, 126) although it was found that frequent operator intervention was required. The low signal-to-noise ratio of $[^{15}O]H_2O$ scans, however, may affect extraction of

the various factors, thereby possibly affecting quantitative accuracy of MBF. Cluster analysis (118), k-means++ clustering (151, 152) and factor analysis of dynamic sequences (FADS) (121) can be used as alternative segmentation algorithms. There are a number of prerequisites for a segmentation algorithm to be feasible for clinical use. Firstly, it should yield blood TACs that result in MBF values, which agree well with those obtained using manually defined blood TACs. Furthermore, segmentation reproducibility should be high, i.e. each segmentation of a single data set should yield the same flow value, Finally, it should be able to segment data reliably without or only with minimal operator intervention.

When arterial and RV TACs are available, segmental MBF can be calculated. Calculating MBF for heart segments has the obvious drawback of losing all information about the distribution of MBF within those segments. As an alternative, kinetic analyses can be performed for each voxel individually, thereby generating parametric MBF images. The gold standard for kinetic analysis, nonlinear least-squares regression (NLR), is slow and very sensitive to noise, making it unsuitable for generating parametric images. The basis function method (BFM) (128) is a much faster and less noise-sensitive method, as it linearizes the model equation and solves it for each voxel using standard linear regression applied to a limited number of predefined possible values of MBF. Its use for $[^{15}O]H_2O$ scans has been reported (132) although the high noise level of $[^{15}O]H_2O$ images on dedicated 2D PET scanners with BGO detectors essentially ruled out calculation of MBF at the voxel level, as resulting parametric MBF images were very noisy (131). Improved scanning statistics of current generation 3D-only clinical PET-CT scanners (66) utilizing LSO or LYSO detectors and faster electronics, however, might result in parametric images of improved quality. Implementation of a correction for RV spill-over (107), which has not been reported before in combination with parametric MBF images, may further improve quantitative accuracy of MBF images, especially in the septum.

The aim of this study was to develop a method for generating quantitative parametric MBF images of diagnostic quality with minimal user intervention. To this end the use of a basis function method, incorporating right ventricular spill-over, was assessed after which quantitative accuracy and reproducibility of four different segmentation algorithms for definition of blood pool TACs were compared using data acquired on a clinical 3D PET-CT scanner.

3.2 Materials and methods

3.2.1 Patients

Data were obtained from a cohort of patients, who were evaluated for coronary artery disease and therefore referred for CT angiography and MBF measurements. A total of 19 consecutive patients (9 men, age range 50–77 y, mean age 65 y; 10 women, age range 31–78 y, mean age 60 y), were included. None of the patients had a documented history of coronary artery disease. Elec-

trocardiography did not show signs of a previous myocardial infarction, and echocardiography showed a normal left ventricular function without wall motion abnormalities in all patients.

3.2.2 Image acquisition

Scans were performed on a Gemini TF 64 PET-CT (Philips Healthcare, Best, The Netherlands) (66). A 5 mL bolus injection of 370 MBq $[^{15}O]H_2O$, followed by 35 mL saline (total duration 23 s), was administered simultaneously with the start of a list-mode emission scan of 6 minutes. The injected dose was chosen to remain within the linear range of the scanner, the upper limit of which is at a singles count rate of about 35 Mcps (153). Singles count rates in the present study were approximately 32 Mcps during the first pass of the bolus. A slow low-dose CT scan (LD-CT, 55 mAs, rotation time 1.5 s, pitch 0.825, collimation 16x0.625, acquiring 20 cm in 37 s compared to 5 s for a regular LD-CT) was performed after each emission scan to correct for attenuation. The emission scan was reconstructed into 22 frames (1x10, 8x5, 4x10, 2x15, 3x20, 2x30 and 2x60 s) using the 3D Row Action Maximum Likelihood Algorithm (3D-RAMLA), applying all appropriate corrections. Images consisted of 45 planes of 144x144 voxels with voxel dimensions of 4x4x4 mm. Two $[^{15}O]H_2O$ scans were performed sequentially: one under adenosine induced stress conditions, the other under rest conditions. Adenosine infusion was started 2 minutes prior to injection of $[^{15}O]H_2O$ and continued during the LD-CT following the stress scan. The time between both $[^{15}O]H_2O$ injections was approximately 20 minutes to allow for decay of radioactivity.

3.2.3 Manually drawn blood VOIs

Using CAPP software (Siemens/CTI, Knoxville), 1 cm diameter regions of interest (ROIs) were placed over the centre of the ascending aorta in at least 10 transaxial image planes in the frame showing the first pass of the injected bolus, as described previously (96). These ROIs were combined into one volume of interest (VOI) for the ascending aorta. A second set of ROIs was placed over the RV cavity in at least 5 transaxial planes, with ROI boundaries at least 1 cm from the RV wall to avoid spill-over of myocardial activity. Again, these ROIs were combined into one RV VOI. Both VOIs were then transferred to the full dynamic images to obtain $C_A(t)$ and $C_{RV}(t)$.

3.2.4 Parametric images

Parametric MBF images were generated using a basis function implementation (128,131,132) of the single tissue compartment model with corrections for spill-over and partial volume effects (12,107):

$$C_T(t) = PTF \cdot MBF \cdot C_A(t) \otimes e^{-\frac{MBF}{V_T} \cdot t} + V_A \cdot C_A(t) + V_{RV} \cdot C_{RV}(t) \qquad (3.1)$$

V_A represents arterial blood volume and left ventricular spill-over fraction, V_{RV} RV spill-over fraction, and V_T the partition coefficient of water in myocardial tissue, which was fixed to 0.91 mL·g^{-1} (11). The last two terms of the model are used to correct for spill-over effects, whilst PTF is used to correct for partial volume effects. A set of 30 basis functions was pre-computed using logarithmically spaced values of MBF_i between 0.1 to 1.8 mL·g^{-1}·min^{-1} for rest scans and 0.1 to 4.5 mL·g^{-1}·min^{-1} for stress scans:

$$B_i(t) = MBF \cdot C_A(t) \otimes e^{-\frac{MBF_i}{V_T} \cdot t} \tag{3.2}$$

The linear combination of the three terms in equation (3.1), resulting in the minimal sum of squared differences, yielded PTF, MBF, V_A and V_{RV}. In voxels with PTF < 0.25 or $V_A + V_{RV} > 0.75$, MBF was set to zero in order to avoid spurious noise-induced high MBF values outside the heart or in blood vessels.

3.2.5 Segmentation algorithms

For segmentation of dynamic data, four different algorithms were used. Cluster analysis (118) iteratively computes, for each voxel, the probability that it belongs to one of the clusters, each of which is described by a multinomial distribution with a mean and variance TAC. Mean and variance of each cluster are calculated using probability weighted voxel TACs, after which new probabilities are calculated. The final probability maps are used for further analysis. Factor analysis of dynamic structures (FADS) (121) uses simple matrix calculations and positivity constraints to iteratively calculate factor images rather than probability densities. Factor analysis (119, 120) also uses matrix calculations and positivity constraints. However, calculations are performed on a new affine space defined using principal component analysis rather than the raw dynamic data. K-means++ (152) is a modified version of K-means clustering (151), which groups voxel TACs iteratively in clusters using the squared sum of differences (i.e. distances) between voxel and TACs. Each voxel is assigned to one cluster in order to minimize the distances within a cluster and maximize the distances between clusters. K-means++ uses different starting values, thereby increasing calculation speed and reliability. In the present study, a corner voxel, located outside the patient, was used as first cluster centre.

Obtained factor or cluster images were normalized such that the sum of all factors and clusters was 1 for each pixel, after which they were thresholded, assigning voxels to only one factor or cluster. For k-means++ clustering, thresholding was not needed, as k-means++ already assigns voxels to only one cluster. Thresholded images were displayed in 3D and, after visual inspection, arterial and RV factors or clusters were assigned manually. Next, to reduce partial volume and spill-over effects, arterial and RV factors or clusters were morphologically eroded once, removing both the outer layer of voxels and possible isolated voxels. The average TACs of the remaining voxels were used as $C_A(t)$ and $C_{RV}(t)$. Each algorithm was tested for 4 to 7 factors or clusters. Prior to analysis, to prevent memory issues, dynamic data were cropped to

extract images of 28x28x18 cm located around the heart using fixed cropping parameters.

3.2.6 Data analysis

Validation of parametric images. Parametric PTF images were rotated in order to obtain short-axis images of the heart. Next, the same transformation was performed to the original dynamic $[^{15}O]H_2O$ data. Myocardial segment VOIs according to the 17-segment model of the American Heart Association were drawn manually on the PTF short axis image. This VOI template was transferred to the short-axis dynamic data to extract segmental $[^{15}O]H_2O$ TACs. These TACs were used to derive MBF for each segment using NLR together with manually obtained $C_A(t)$ and $C_{RV}(t)$. Corresponding parametric MBF values were obtained by transferring the same VOI template to the parametric MBF images. Correlation and agreement between both sets of segmental MBF values and of coronary flow reserve (CFR, defined as stress MBF divided by rest MBF) was assessed using Deming regression, intra-class correlation coefficients (ICC) and Bland-Altman analysis (154).

Validation and reproducibility of segmentation methods. Segmental MBF was derived from corresponding TACs using NLR and the various $C_A(t)$ and $C_{RV}(t)$ obtained from all segmentation algorithms. Correlation and agreement of these MBF and corresponding CFR values with those obtained from manually defined $C_A(t)$ and $C_{RV}(t)$ were assessed using Deming regression, intra-class correlation coefficients (ICC) and Bland-Altman analysis. Segmentation reproducibility was only assessed for the number of factors that showed the highest correlation with manually derived blood curves. $C_A(t)$ and $C_{RV}(t)$ were determined 50 times for both rest and stress scans of three randomly selected patients using each of the algorithms. Using NLR, myocardial segment TACs were fitted for each $C_A(t)$ and $C_{RV}(t)$, after which the coefficient of variation (CoV) of MBF was calculated for each algorithm and used as a measure for segmentation reproducibility.

3.3 Results

3.3.1 Parametric images

One patient showed MBF, as determined by NLR, outside the predefined range used for BFM. For this patient with very high stress MBF, the predefined range of MBF values was adjusted to 0.1-7.2 $mL \cdot g^{-1} \cdot min^{-1}$. In Figure 3.1 parametric MBF images are shown of one patient with a normal flow distribution and another with a stress inducible perfusion defect. Figure 3.2 shows regression and Bland-Altman plots of segmental MBF derived from parametric MBF images against those obtained from NLR analysis of corresponding VOIs. Agreement was high (ICC = 0.984 for MBF) and Bland-Altman plots showed no significant difference between both MBF values (mean difference 0.023, 95% confidence

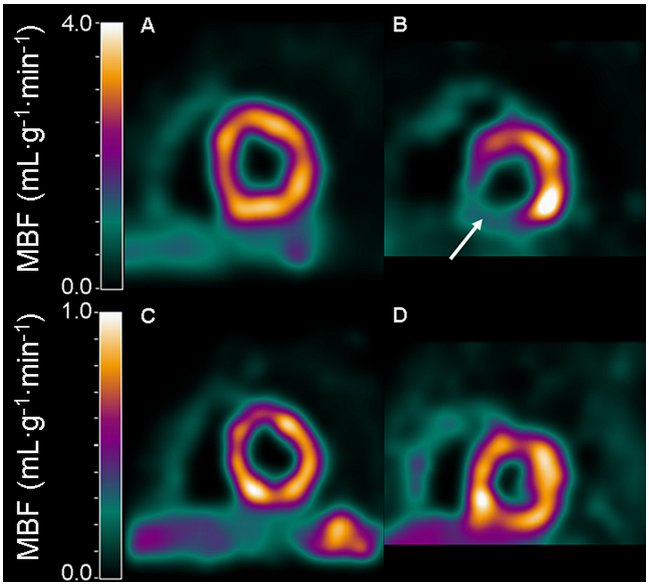

Figure 3.1. *Typical parametric short-axis images of stress (A, B) and rest (C, D) MBF of a patient with no perfusion defects (A,C) and a patient with a stress inducible perfusion defect in the inferior wall (B,D). Images were filtered with a 10 mm Gaussian filter.*

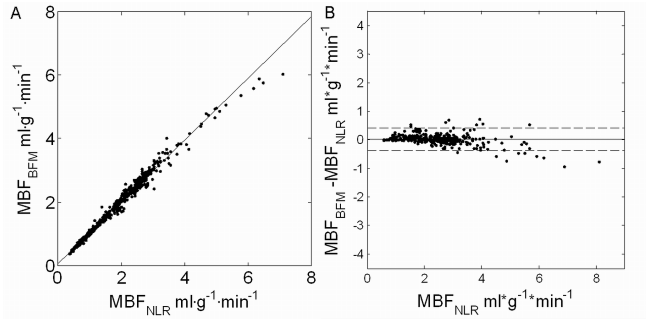

Figure 3.2. *Regression (A) and Bland-Altman (B) plots of segmental MBF derived using NLR applied to corresponding TACs (MBF_{NLR}) versus average parametric MBF (MBF_{BFM}). Continuous lines indicate linear fit in A and mean difference in B, dashed lines indicate mean difference ± 2SD.*

interval -0.355 - 0.401). Deming regression resulted in a slope of 0.977 and and an intercept of 0.046. Both slope and intercept were significantly different from 1 and 0 ($p < 0.05$), respectively, indicating a very small but significant bias in parametric images relative to NLR.

3.3.2 Factor images

On average, all segmentation algorithms took about 20 s on a standard desktop pc with a maximum of 1 min. Factor images without threshold are shown in Figure 3.3. Images obtained using cluster analysis contained many voxels with a value of 1, in contrast to FADS and factor analysis. A threshold of 1 for cluster analysis, 0.5 for FADS and 0.4 for factor analysis yielded 3D images (Figure 3.4), in which structures could clearly be identified. Note that arterial images include left atrium, left ventricle and aorta and that venous images include vena cava superior, right atrium, right ventricle and pulmonary artery. The

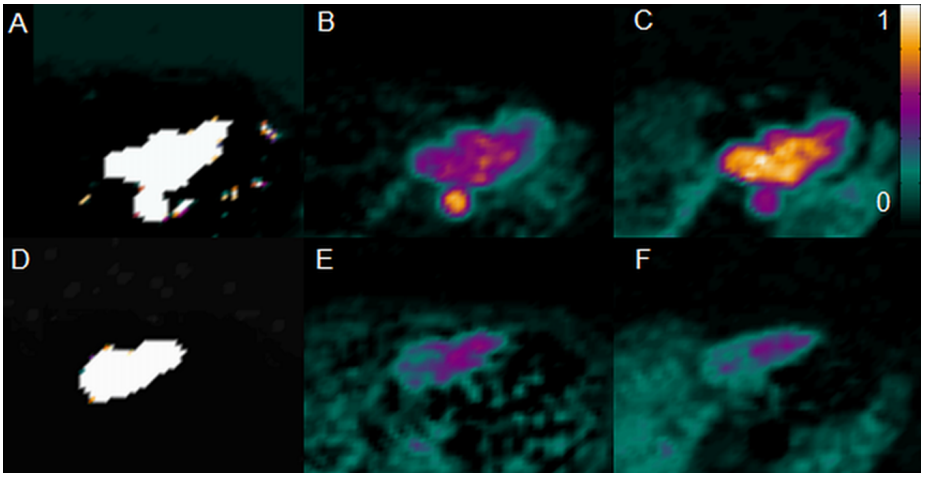

Figure 3.3. *Factor images of arterial (A-C) and RV (D-F) factors obtained using cluster analysis with 6 clusters (A,D), FADS with 7 factors (B,E). and factor analysis with 5 factors (C,F). The colour scale is the same for all images. RV is clearly visible in the factor images obtained using cluster analysis, but less so in images obtained using FADS and factor analysis.*

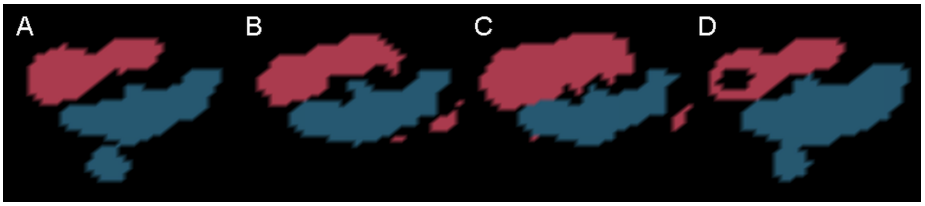

Figure 3.4. *Typical two-dimensional thresholded factor images showing arterial (blue) and venous (red) factors, cropped around the heart. Factor images were obtained using cluster analysis with 6 factors (A), FADS with 7 factors (B), factor analysis with 5 factors (C) and k-means++ using 7 factors (D).*

chosen thresholds yielded arterial clusters of similar size for each segmentation algorithm. The low threshold for FADS and factor analysis resulted in noisy 3D images. FADS and factor analysis generated relatively small RV factors or assigned more than one factor to the RV, making it difficult to extract $C_{RV}(t)$. For factor analysis, occasionally myocardium and RV were combined in one factor, leading to a more difficult extraction of $C_{RV}(t)$.

3.3.3 Correlation with manually defined blood TACs

ICC, slope of deming regression line, mean difference and limits of agreement for MBF and coronary flow reserve (CFR) calculated using each segmentation algorithm and those using manually defined $C_A(t)$ and $C_{RV}(t)$ are listed in Table 3.1, showing high ICC for most methods (ICC > 0.9). Figure 3.5 and 3.6 show corresponding regression and Bland-Altman plots of MBF calculated with each of the segmentation algorithms against MBF based on manually defined $C_A(t)$ and $C_{RV}(t)$. In general, all algorithms yielded high correlation with MBF and

CFR based on manually blood TACs for at least one chosen implementation. For MBF, all regression lines had slopes significantly higher than 1 indicating positive bias. For CFR, slopes were closer to 1 indicating a smaller bias.

Cluster analysis yielded the highest agreement with ICC of 0.977 for MBF when using 6 clusters. In addition, it provided high agreement for all implementations tested, indicating low sensitivity to the chosen number of clusters. FADS showed high agreement with MBF based on manually defined blood TACs when using 5 to 7 factors (ICC of 0.971 for MBF when using 7 factors). For factor analysis, it was not possible to segment all patients correctly using a fixed number of factors. In addition, quantitative results were very sensitive to the number of factors used. Five factors yielded the highest agreement (ICC of 0.940 for MBF). In addition, this number of factors appeared to be the most generally applicable for the patients included. For stress scans, k-means++ persistently included myocardial voxels in the arterial factor, resulting in large overestimations of both stress MBF and CFR. Nevertheless, agreement with MBF based on manually defined blood TACs was high (ICC of 0.886 for MBF, when using 7 clusters).

3.3.4 Segmentation reproducibility

Segmentation reproducibility was assessed for cluster analysis with 6 clusters, FADS with 7 factors, factor analysis with 5 factors and k-means++ with 7 clusters. CoVs are shown in Table 3.2. As can be seen, both k-means++ and

Table 3.1. *ICC, slope of Deming regression, mean difference and limits of agreement of Bland Altman plots between MBF and CFR obtained using each algorithm and corresponding values for manually obtained TACs. Slopes marked with an asterisk (*) differ significantly from 1 ($p < 0.05$).*

		MBF				CFR			
		ICC	Slope	Mean difference	Limits of agreement	ICC	Slope	Mean difference	Limits of agreement
Cluster analysis	4	0.859	1.635*	0.509	-0.923 – 1.942	0.900	1.334*	0.291	-0.841 – 1.423
	5	0.927	1.286*	0.306	-0.571 – 1.184	0.951	0.938*	0.091	-0.568 – 0.750
	6	0.977	1.150*	0.209	-0.256 – 0.675	0.985	0.971*	-0.014	-0.386 – 0.358
	7	0.974	1.155*	0.182	-0.315 – 0.678	0.975	0.928*	0.04	-0.425 – 0.504
FADS	4	0.870	1.25*	0.341	-0.854 – 1.536	0.618	1.462	0.22	-1.993 – 2.433
	5	0.953	1.183*	0.219	-0.453 – 0.891	0.950	1.021	0.116	-0.573 – 0.806
	6	0.946	1.219*	0.212	-0.521 – 0.946	0.945	1.030	0.137	-0.591 – 0.864
	7	0.971	1.163*	0.185	-0.342 – 0.713	0.974	0.959*	0.043	-0.442 – 0.528
Factor analysis	4	0.683	1.882*	0.504	–1.769 - 2.776	0.641	2.436*	0.332	-1.959 – 2.603
	6	0.927	1.339*	0.225	-0.677 – 1.127	0.918	1.048*	0.149	-0.809 – 1.108
	5	0.940	1.278*	0.290	-0.508 – 1.087	0.953	1.187*	0.124	-0.558 – 0.805
	7	0.397	3.457*	0.781	-3.393 – 4.956	0.356	1.613*	0.129	-3.004 – 3.263
K-means	4	0.638	1.928*	0.998	-1.530 – 3.527	0.607	1.769*	0.519	-2.002 – 3.040
	5	0.833	1.703*	0.701	-0.906 – 2.309	0.801	1.542*	0.527	-1.208 – 2.262
	6	0.876	1.613*	0.585	-0.752 – 1.921	0.920	1.269*	0.327	-0.662 – 1.316
	7	0.886	1.563*	0.499	-0.755 – 1.754	0.929	1.226*	0.274	-0.634 – 1.182

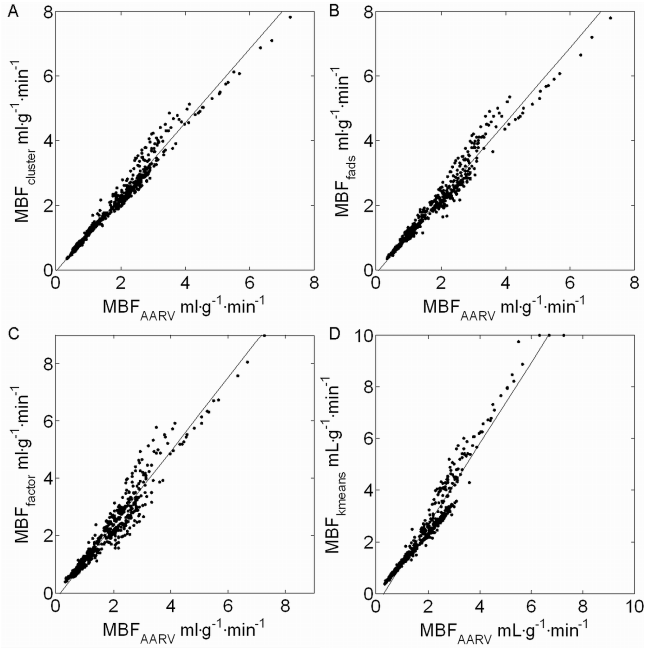

Figure 3.5. *Regression plots of segmental MBF calculated using cluster analysis with 6 clusters (A), FADS with 7 factors (B), factor analysis with 5 factors (C) and k-means++ with 7 clusters (D) with MBF calculated using manually obtained CA(t) and CRV(t). Lines indicate a linear fit with zero intercept.*

factor analysis yielded identical results for repetitive analyses, which is inherent to these methods. Cluster analysis and FADS, which both require random initial values, showed a small variation between repetitive analyses (CoV in MBF $< 5\%$ and $< 8\%$ for cluster analysis and FADS, respectively). In a limited number of cases ($< 5\%$ of the total), cluster analysis was found to fail in separating aorta and left ventricle from myocardial tissue. This segmentation error was obvious in the 3D cluster images, and these cases were therefore removed after visual inspection of the cluster images. Repeating the segmentation reproducibility test after excluding these cases resulted in a reduction in CoV.

3.4 Discussion

In the present study four different algorithms for automatically segmenting blood pool TACs were compared. In addition, a basis function method for generating absolute MBF parametric images, incorporating both LV and RV spill-over corrections, was validated.

Agreement of average segmental MBF and CFR, derived directly from parametric images, with segmental MBF and CFR derived using NLR, was high. This indicates that it is possible to generate quantitatively accurate parametric MBF images using the BFM implementation proposed, together with manually obtained $C_A(t)$ and $C_{RV}(t)$. Slope of the Deming regression was 0.977 and was significantly different from 1, indicating a small but significant underestimation of MBF in parametric images. However, an underestimation as small as 2.3%

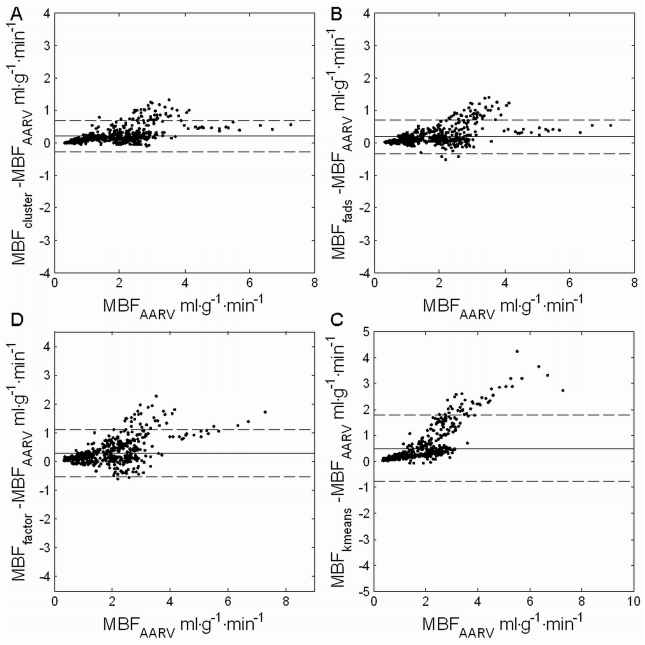

Figure 3.6. *Bland Altman plots of segmental MBF calculated using cluster analysis with 6 clusters (A), FADS with 7 factors (B), factor analysis with 5 factors (C) and k-means++ with 7 clusters (D) with MBF calculated using manually obtained CA(t) and CRV(t). Continuous lines indicate mean difference, dashed lines mean ± 2SD.*

in the parametric images can be considered irrelevant for clinical practice and therefore this was considered not an issue for quantification of MBF. Generated images (Figure 3.1) were of diagnostic quality. For one patient, the predefined range of possible MBF values had to be increased due to a high stress MBF. However, stress MBF $>$ 4.4 mL·g^{-1}·min^{-1} can be considered to be outside the clinically relevant range of MBF, as stress MBF below 1.5-2.5 mL·g^{-1}·min^{-1} (the actual level being dependent on age) is generally considered to be ischemic (21), and therefore this issue should have no influence on clinical diagnosis.

Agreement between all segmentation algorithms and manually obtained blood curves was high (ICC $>$ 0.9 for at least one number of clusters or factors), with

Table 3.2. *Coefficients of variation (CoV) of all segmentation methods obtained by calculating input functions and perfusion values 50 times for 3 patients each. Factor analysis and k-means++ showed exactly the same results when repeating calculations. Cluster analysis and FADS showed a higher CoV for stress scans than for rest scans. When the success of each cluster analysis was assessed visually and failures were restarted, CoV of cluster analysis decreased.*

CoV (%)	Rest	Stress
Cluster analysis	3.39	4.76
Cluster analysis excluding failed analyses	2.29	3.24
FADS	4.98	7.74
Factor analysis	0	0
K-means++	0	0

the highest agreement obtained for cluster analysis with 6 clusters (Table 3.1). The segmentation reproducibility of each algorithm was very good to excellent with CoVs of MBF $< 5\%$ for cluster analysis, $< 8\%$ for FADS and, inherently, 0% for both factor analysis and k-means++. Each algorithm overestimated MBF compared to MBF based on manually defined blood pool TACs. A possible explanation is the fact that manually obtained TACs were derived from a small volume in the ascending aorta. In contrast, the segmentation algorithms included the entire left ventricle, ascending aorta and descending aorta (Figure 3.4). This larger volume introduces dispersion and partial volume effects in $C_A(t)$, resulting in higher apparent MBF compared to MBF based on a manually defined AA TAC. To verify this, $C_A(t)$ was also obtained from manually drawn ROIs over both ascending aorta and left ventricle, which showed a similar effect on MBF (data not shown). This effect was much smaller for CFR (Table 3.1), indicating that relative overestimations in stress and rest MBF were similar and cancelled out when calculating CFR.

Each algorithm had its own shortcomings. Occasionally ($< 5\%$ of cases), cluster analysis failed to separate aorta from myocardium. When looking at the 3D images, however, it was easy to determine whether the analysis succeeded or failed. Consequently, due to the random starting values, a failed analysis could easily be resolved by restarting the analysis using the same number of clusters. Although this meant that the method sporadically required user intervention, this was not considered a major drawback of cluster analysis due to the ease of determining the success or failure of an analysis.

An important drawback of k-means++ is that it persistently included myocardial voxels in the arterial factor when segmenting stress scans, resulting in large overestimations of both stress MBF and CFR. This problem was independent of the number of clusters used.

FADS and factor analysis were unable to segment the RV correctly, resulting in incorrect spill-over corrections. Furthermore, in contrast to cluster analysis, a low threshold had to be applied to the factor images obtained with both FADS and factor analysis, resulting in noisy images and inclusion of voxels that belonged for up to 60% to other factors. The effects of this on absolute MBF values, however, were small as seen in Table 3.1.

As described previously, it is essential to use the correct number of factors when using factor analysis for segmentation (107,125) Similar results were found in the present study. In particular, it was not possible to find a single number of factors that could be used for segmenting all patients. As frequent user intervention, i.e. manually changing the number of factors, is required to prevent erroneous results, factor analysis was not considered feasible for clinical use. El Fakhri et al. (155) presented a method that modifies factors and factor images after analysis by penalizing overlap in factor images. This method has not been tested in the present study, as cluster analysis did not suffer from overlap in factor images and provided good results. Furthermore, post-processing was not expected to improve feasibility of factor analysis, as incorrect segmentations were not expected to be corrected by penalizing overlap.

A limitation of the present study was that, in order to prevent memory

issues during analysis, data were cropped around the heart using fixed parameters. The choice of these parameters and additional pre-processing may affect the optimal number of clusters. When different pre-processing steps are incorporated, the optimal number of clusters should be reassessed. Nevertheless, as cluster analysis was insensitive to the number of clusters chosen, this effect may be small.

3.5 Conclusion

This study demonstrates that it is possible to generate good quality parametric images of absolute MBF using $[^{15}O]H_2O$ and a clinical PET-CT scanner. This can be achieved with minimal user intervention by using automatic definition of blood pool TACs and on a basis function method including right ventricular spill-over correction for calculation of parametric MBF images. Cluster analysis with 6 clusters proved to be the best segmentation algorithm for automatic definition of blood pool TACs, resulting in high correlation and agreement of MBF values with those based on manually defined blood pool VOIs. Consequently, absolute MBF images, generated from a $[^{15}O]H_2O$ scan, are now available for clinical use.

Acknowledgements

The authors would like to thank Suzette van Balen, Judith van Es, Amina Elouahmani, Femke Jongsma, Nazerah Sais en Annemiek Stiekema for scanning patients, and Dr. Gert Luurtsema, Robert Schuit, Kevin Takkenkamp and Henri Greuter for production of $[^{15}O]H_2O$. This work was supported financially by Philips Healthcare.